

# Effect of Microstructure on Tensile Properties of Electrospark Deposition Repaired Ni-superalloy

Pablo D. Enrique <sup>\*a</sup>, Zhen Jiao <sup>b</sup>, Norman Y. Zhou <sup>a</sup>, Ehsan Toyserkani <sup>a</sup>

<sup>\*</sup>Corresponding author: [pdenriqu@uwaterloo.ca](mailto:pdenriqu@uwaterloo.ca)

<sup>a</sup> University of Waterloo, 200 University Ave W, Waterloo, Ontario, N2L 3G1, Canada.

<sup>b</sup> Huys Industries Ltd., 175 Toryork Drive, Unit 35 Weston, Ontario, M9L 1X9, Canada.

---

**This is an author generated post-print of the article:**

P.D. Enrique, Z. Jiao, N.Y. Zhou, E. Toyserkani, Effect of Microstructure on Tensile Properties of Electrospark Deposition Repaired Ni-superalloy, Mater. Sci. Eng. A (2018). doi:10.1016/j.msea.2018.05.049.

This manuscript version is made available under a [CC-BY-NC-ND 4.0](https://creativecommons.org/licenses/by-nc-nd/4.0/) license.

The final citeable publication can be found here: <https://doi.org/10.1016/j.msea.2018.05.049>

## Abstract

Cavities introduced to Inconel 718 tensile specimens were repaired with the use of electrospark deposition (ESD) and tensile properties of repaired specimens were investigated. Reduced energy input during ESD resulted in a larger number of splat boundaries and greater yield strength recovery during tensile testing. Analysis of the fracture surface showed a trans-splat and inter-splat crack propagation pathway, with splat boundaries exhibiting lower fracture toughness than material within the splats. Changes in crack propagation direction were attributed to grain growth across splat boundaries and brittle secondary phases forming within splats during ESD.

*Keywords: Electrospark deposition; Nickel superalloy; Tensile properties; Fracture behaviour*

---

## 1. Introduction

The use of electrospark deposition (ESD) for the repair of damaged components is often proposed and investigated in literature [1,2]. Most applications focus on expensive components for which no other cost-effective or high-quality process exists. Oftentimes, the detrimental effects of heat affected zone formation, residual stresses and welding induced distortion limits the type of repair process that can be used. These effects can be mitigated through ESD repair techniques [3]. For this reason, aerospace and energy industries are common targets for the application of ESD, in which many high performance and high cost materials are subjected to extreme operating conditions. These applications include the repair of gas turbine engine blades suffering from issues such as chipped or damaged coatings, and dimensional restoration of out-of-tolerance manufactured parts [3]. This avoids completely replacing or scrapping the affected components, providing an economic incentive for the implementation of an ESD repair process.

The ESD micro-welding process makes use of a consumable electrode deposited onto a conductive substrate through a series of short-duration electrical sparks. Material transfer results in splats that rapidly solidify and undergo metallurgical bonding with the substrate. The short pulse duration often results in minimal heat affected zones [1], unlike other traditional welding processes. Previous studies conducted for the ESD repair of nickel-based superalloy materials have found favourable deposition properties with respect to the substrate material and other repair techniques. Wear and tensile test results of repaired Inconel 718 substrates show that wear rate, yield strength and ultimate strength were similar to the base metal, although reductions in ductility were observed during tensile testing [3]. This was also observed for other nickel based alloys; a comparison of repair techniques for Waspaloy show that ESD is able to achieve a higher ultimate strength at the expense of a significant reduction in ductility [4].

Although mechanical properties have been reported previously, a study on the effect of microstructure on tensile properties in ESD repaired substrates is required to understand the failure mechanism of ESD repaired components. Analysis of crack propagation during tensile testing has the potential to improve ESD process parameter optimization for applications that require good mechanical properties. Interpretation of tensile testing data for ESD repaired specimens is performed, with a focus on the effect of microstructure on mechanical properties and crack propagation pathways. Results indicate that lower energy parameters result in higher yield strength, likely a result of increased splat boundaries and finer microstructure features. However, splat boundaries are found to serve as crack propagation pathways during fracture, which – along with the formation of brittle interdendritic phases – contribute to the lower recovery in ultimate strength.

## 2. Materials and Methods

Double edge notched tensile testing specimens were made from a 3.3 mm thick Inconel 718 solution-annealed sheet. The supplier provided composition is listed in Table 1, and the specimen dimensions with and without a cavity are shown in Figure 1.

**Table 1.** Inconel 718 Substrate Composition (wt%)

Ni	Fe	Cr	Nb	Mo	Ti	Co	Al	C	Mn	Si	Cu
53.5	17.8	18.5	5.1	2.9	0.9	0.2	0.6	0.03	0.09	0.08	0.13

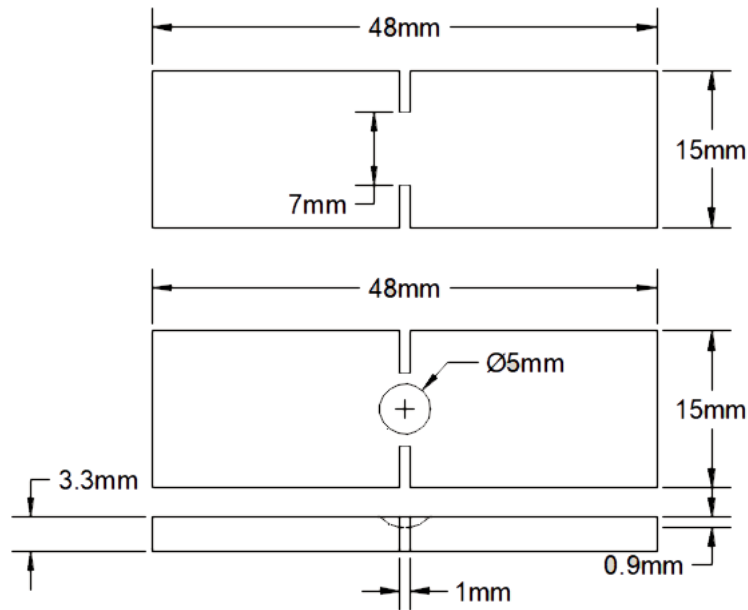


**Figure 1.** Schematic of tensile testing specimens with and without a cavity

Cavities with ideal dimensions of 5 mm in diameter and 0.9 mm deep (seen in Figure 1) were machined with the use of a ball nose end mill. Cavities were then repaired with a Huys Industries ESD machine using a 3.2 mm diameter Inconel 718 electrode. Local shielding was provided by ultra-pure Argon gas at a flow rate of 10 L/min. A hand-held motorized peening tool is used throughout the deposition to reduce surface roughness, and an aluminum oxide grinding stone is used to perform dimensional restoration of the filled cavities.

The ESD parameters used for the cavity repair are listed in Table 2, with the input energy per pulse ( $E_i$ ) calculated using the standard formula for energy stored in a capacitor,

$$E_i = \frac{1}{2} CV^2 \quad (1)$$

where  $C$  is the capacitance and  $V$  is the voltage.

**Table 2.** ESD Parameters for Cavity Repair

Parameters	Energy Input	
	Low	Medium
Voltage (V)	50	100
Capacitance ( $\mu\text{F}$ )	80	80
Frequency (Hz)	170	170
Input Energy (mJ)	100	400

Three types of tensile testing specimens are created and tested: base metal specimens have no cavities, empty cavity specimens contain cavities which have not been repaired, and repaired specimens consists of cavities which have been filled with Inconel 718 via ESD. These specimens are tested to failure on an Instron model 4206 at a constant extension speed of 1 mm/min. A total of 3 base metal specimens, 3 low energy repaired specimens and 6 medium energy repaired specimens are tested. Of the 6 medium repaired specimens, 4 are tested to failure and 2 are tested until a crack begins to form. Yield strength values - but not ultimate strength - are obtained from the incomplete tests, and independent t-tests with two-tailed hypothesis are performed to evaluate differences in the mean values between low energy, medium energy and base metal specimens. A 90% confidence level is used to identify significance ( $p < 0.1$ ) and the effect size is evaluated with the use of a corrected Hedges'  $g$  value for small sample sizes [5], where  $g = 0.8$  is considered a large effect and  $g = 1.3$  is considered a very large effect [6,7]. Due to small sample sizes typically associated with tensile test studies and potential variability in repair quality between samples, some traditionally non-statistically significant results ( $0.05 < p < 0.1$ ) with large effect sizes ( $g > 0.8$ ) are investigated due to the increased potential of type II errors in small samples and the independence of effect size from sample size [6].

Fractured samples are imaged with a JEOL JSM-6460 scanning electron microscope (SEM) and cross sections of the fracture surface are imaged with an Oxford BX51M optical microscope (OM). Microhardness measurements are performed with the use of a Wolpert Wilson 402 MVD micro Vickers hardness tester. Cross sectioned surfaces are polished and then etched with inverted glycergia (HCl:HNO<sub>3</sub>:Glycerol in a 5:1:1 ratio) for 1.5 to 2.5 minutes.

### 3. Results

#### 3.1. ESD Microstructure

Initial observations of ESD repaired Inconel 718 cavities prior to tensile testing reveal the build-up mechanism of the repair process. Upon cross sectioning and etching with inverted glycergia, the individual splats from the ESD repair are visible. Figure 2b shows various sized splats which stack together to form the deposited material that comprises the repaired cavity in Figure 2a.

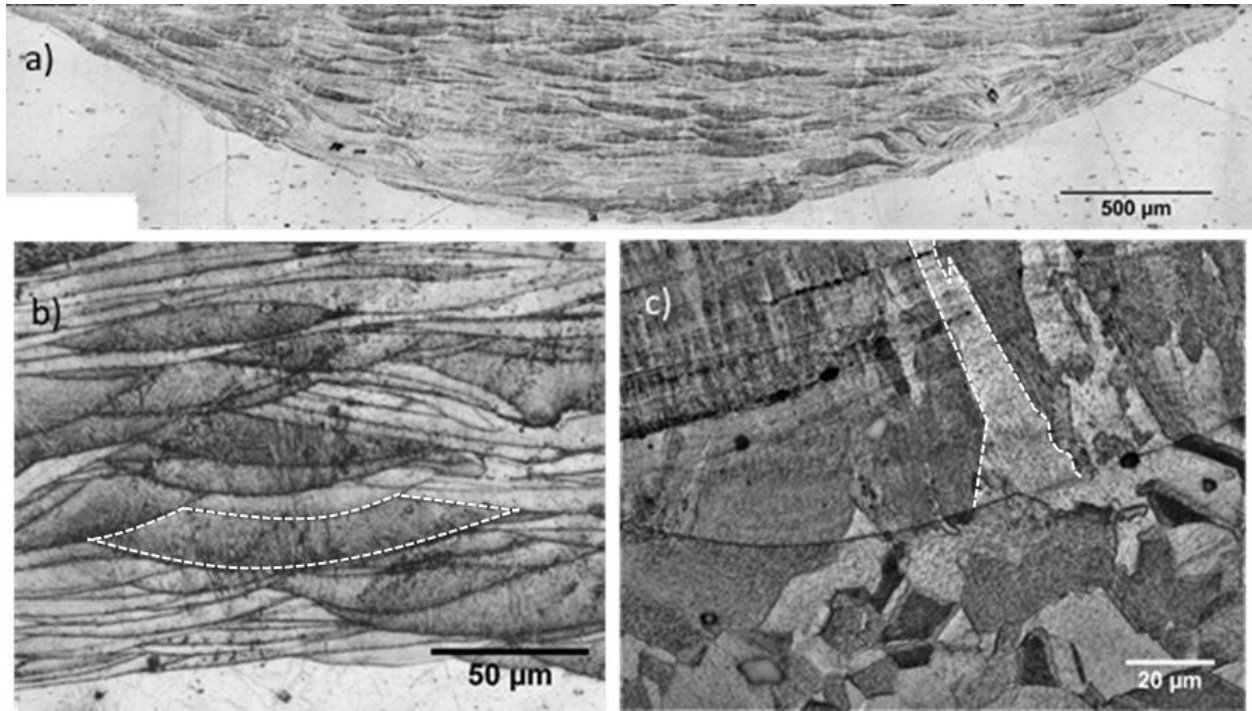


**Figure 2.** Cross sectional OM image after etching of **a)** a repaired cavity, **b)** the deposition splats within a repaired cavity (one splat highlighted with dashed lines) and **c)** epitaxial grain growth (one epitaxial grain highlighted with dashed lines) in deposited material influenced by the substrate base metal grain

The layered microstructure resembles that of other ESD processed materials and has been documented in depth in literature studies [1]. The deposition parameters listed in Table 2 were chosen to minimize the defects commonly observed within ESD, including voids, cracks and delamination. An average density of 99.35% was determined from OM images of cross-sectioned cavities, with no significant difference between medium and low energy ESD parameters. Longer etching times reveal epitaxial grains within the deposited material, some of which traverse splat boundaries in the direction of material buildup, as shown in Figure 2c. The volume of the deposited splat is related to the input energy per pulse, with larger quantities of deposited material resulting in thicker deposition splats [8]. It is expected that the average splat thickness of a deposition performed with medium energy input is larger than that of a low energy input deposition, such that fewer splat layers are required to fill a cavity. Measurements of 140 splat thicknesses showed that medium energy deposition splat thickness ( $11.2 \mu\text{m}$  with a standard error of  $\pm 2.0 \mu\text{m}$  and a maximum measured splat thickness of  $95.3 \mu\text{m}$ ) was larger than that of low energy depositions ( $7.1 \mu\text{m}$  with a standard error of  $\pm 0.6 \mu\text{m}$  and a maximum measured splat thickness of  $33.4 \mu\text{m}$ ). This corresponds with the time required for the repair of a cavity; medium energy ESD parameters required 18 minutes while low energy parameters required 64 minutes on average.

The cellular dendritic subgrain structure and interdendritic phases of ESD processed Inconel 718 have been previously reported in literature [9], resembling that of other rapid solidification processes [10]. The effect of splat size on microstructure features can be seen in Figure 3, with larger cellular dendritic subgrains in the thicker splat.

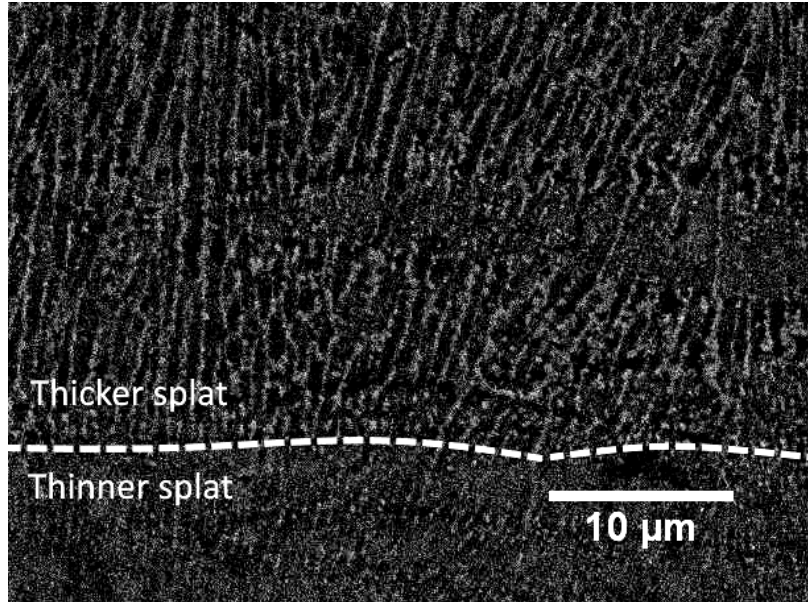


**Figure 3.** SEM image of subgrain microstructure in ESD processed Inconel 718 after etching

Interdendritic regions appear lighter in the SEM due to edge effects from faster etching of the  $\gamma$  phase and slower etching of interdendritic secondary (Laves and carbide) phases [10]. Interdendritic Laves regions were previously reported to be 50 nm in diameter [11]. However, the diameter of interdendritic phase segregation in ESD appears to be influenced by splat size. Thicker splats show larger diameter interdendritic regions when compared to thinner splats, likely due to lower cooling rates during and after solidification resulting in coarser microstructure features.

### 3.2. Mechanical Properties

Repaired tensile specimens are tested to failure and the mechanical properties are compared to base metal specimens and empty cavity specimens. Average results from these tests are shown in Table 3, with representative tensile test curves shown in Figure 4b. The standard formula for stress ( $\sigma$ ) is seen in Equation 2,

$$\sigma = \frac{F}{A} \quad (2)$$

where  $F$  is the applied force and  $A$  is the cross-sectional area of the specimen. For the calculation of stresses in Table 3, the original cross-sectional area ( $A_0$ ) was used, which assumes no cavity was made. As a result, the empty cavity specimens decrease in strength when compared to base metal specimens by an amount equivalent to the reduction in cross-sectional area at the specimen's fracture plane. The recovery in yield and ultimate strength of repaired specimens when compared to empty cavity specimens can be attributed to the ESD material. The yield and ultimate strengths obtained by Carofalo et al. [4] for ESD repaired specimens were approximately -2% and -9% respectively when compared to base metal specimens, which closely compares to results obtained in this study (shown in Table 3).

**Table 3.** Tensile Test Results and Relative Performance (RP) Compared to Base Metal Specimens

Specimen Type	Yield Strength		Ultimate Strength	
	MPa	RP	MPa	RP
Base Metal	605		853	
Empty Cavity	508	-16%	743	-13%
Repaired (Med)	586	-3%	777	-9%
Repaired (Low)	632	+5%	791	-7%

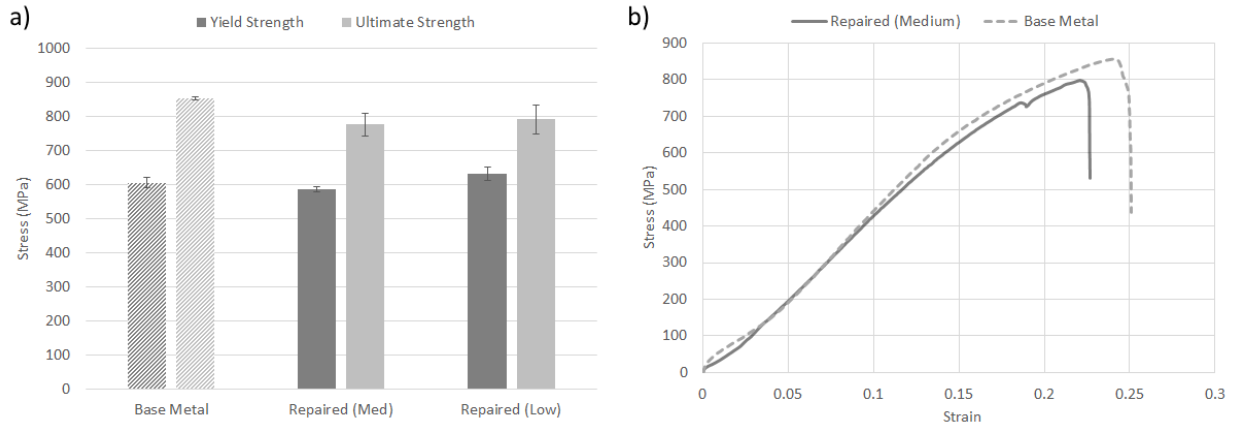


**Figure 4. a)** Yield and ultimate strengths with standard error and **b)** representative stress-strain curves

No significant difference exists between the yield strength of base metal specimens and low energy repaired ( $p=0.334$ ) or medium energy repaired ( $p=0.275$ ) specimens. However, repairs performed using low energy input achieved higher yield strengths than those with medium energy input ( $p=0.066$ ) and displayed a very large effect size ( $g=1.31$ ). Unlike the recovery in yield strength, the difference in ultimate strength between base metal and repaired specimens remains statistically significant ( $p=0.030$ ) and displays a large effect size ( $g=1.14$ ). Figure 4b shows the stress-strain curve of an ESD repaired tensile specimen using medium energy input, which exhibits a lower ultimate strength than the base metal and the presence of a pre-failure fracture (deposition fracture).

The first fracture nearer the yield point suggests that a less ductile fracture occurs in the ESD material, followed by greater plastic deformation of the base metal and subsequent ductile fracture. The pre-failure fracture leads to a change in the effective cross-sectional area of the specimen as it undergoes tensile testing. When incorporating the reduction in area due to the presence of an unfilled cavity in empty cavity specimens and the reduction in area due to the deposition fracture in repaired specimens, an adjusted ultimate strength (AUS) for the substrate base metal can be determined. The results presented in Table 4 demonstrate that the fracture of the base metal occurs at similar stresses in all specimen types. This suggests that the ESD repair process did not form a noticeably detrimental heat-affected zone in the base metal, and that the pre-failure fracture of the deposition during tensile testing does not propagate into or weaken the base metal substrate.

**Table 4.** Adjusted Ultimate Strength (AUS) of Tensile Specimen Substrate

Specimen Type	AUS (MPa)
Base Metal	853
Empty Cavity	858
Repaired (Med)	857
Repaired (Low)	862

### 3.3. Fractographic Analysis

The base metal and deposition fracture surfaces were found to exhibit different morphologies. SEM images shown in Figure 5a and 5b display the presence of a dimpled morphology on the base metal fracture surface and step-like facets with smoother surfaces in the deposited material. Cross sectional images of the base metal near the fracture interface (Figure 6a and 6b) show elongation of the grains in the direction of the applied tensile force, consistent with a ductile fracture.

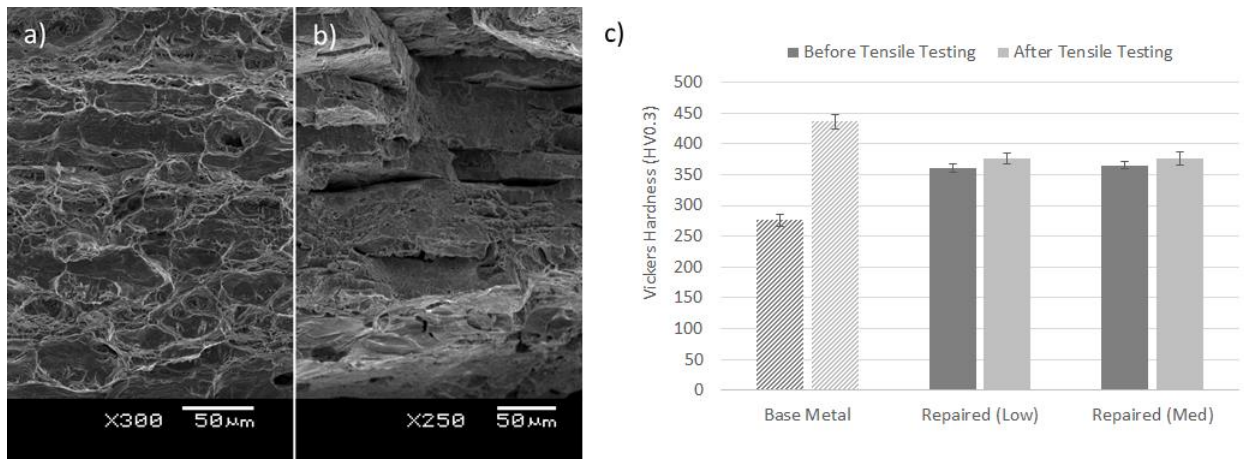


**Figure 5.** SEM image of **a)** base metal fracture surface, **b)** deposition fracture surface with step facets, and **c)** microhardness measurements and standard error of base metal and deposition in repaired specimens within 300  $\mu\text{m}$  of the fracture interface before and after tensile testing

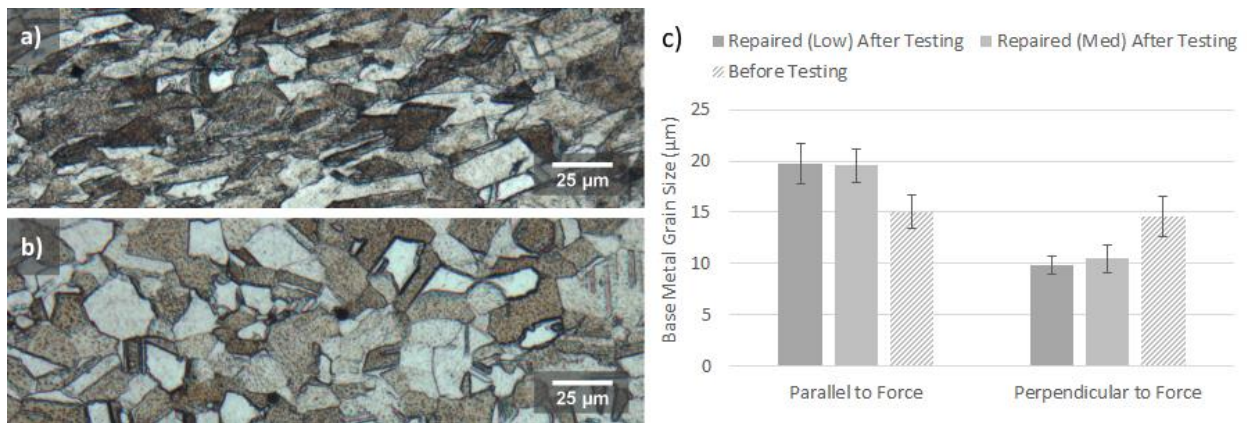


**Figure 6.** Grain structure of Inconel 718 base metal **a)** within 300  $\mu\text{m}$  of the fracture interface, **b)** as received prior to testing and **c)** the grain size and standard deviation in the base metal before and after tensile testing within 300  $\mu\text{m}$  of the fracture interface

Measurement of the grain size for the base metal of repaired specimens show an average 30% elongation along the direction of the applied tensile stress as well as a 31% reduction in grain size along the direction perpendicular to the applied stress (Figure 6c). Microhardness measurements show a significant increase in Vickers hardness (from 276 HV to 436 HV as shown in Figure 5c) for the base metal along the fracture interface after tensile testing. This strain hardening behaviour arises due to a pileup of dislocations in the crystal lattice, which occurs during plastic deformation [12]. Unlike the base metal, the ESD material does not exhibit a significant increase in microhardness, again suggesting that the deposited material does not undergo significant plastic deformation and experiences a more brittle fracture. Microhardness measurements were also performed parallel to the buildup direction on the top surface of medium energy ESD repaired cavities and were compared to results obtained for the perpendicular direction given in Figure 5c. Hardness in the parallel direction (381.0 HV with a standard error of  $\pm 7.2$  HV) was higher than that of the perpendicular direction (365.5 HV with a standard error of  $\pm 5.6$  HV) by 4.2%, indicating the presence of a small hardness anisotropy.

#### 4. Discussion

##### 4.1. Effect of Hardness and Strength Mismatch on Mechanical Properties

Figure 7 shows the crack initiation location at the surface of the ESD Inconel 718, which then proceeds to propagate towards the center of the specimen.

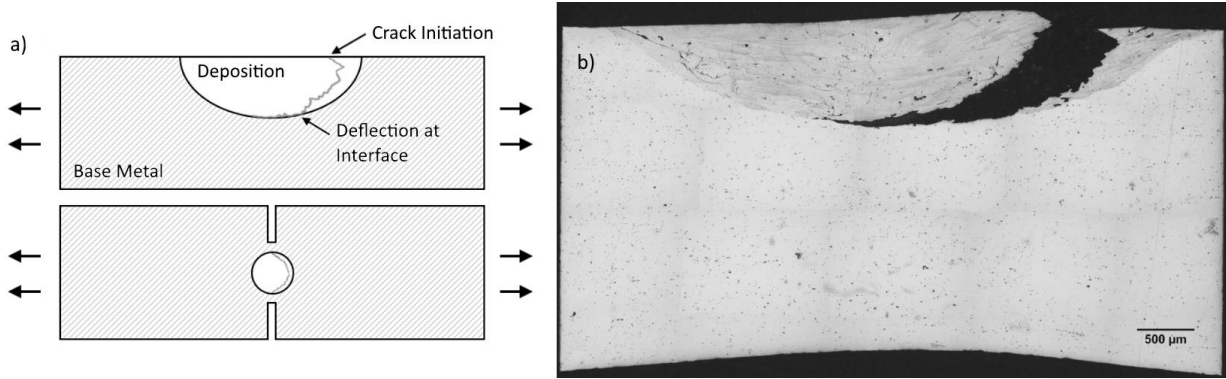


**Figure 7. a)** Side and top view schematic of crack location relative to deposition geometry and **b)** cross-sectional OM image of a lightly etched specimen tested until the initial fracture of the deposited material

A better understanding of failure in welded systems can be obtained by calculating the extent of mechanical property mismatch between the deposited material and the base metal. The hardness mismatch ratio ( $M$ ) is defined as the ratio between the hardness of the deposited material ( $H_D$ ) and base metal ( $H_{BM}$ ) in Equation 3.

$$M = \frac{H_D}{H_{BM}} \quad (3)$$

Using the average hardness values reported in Figure 5c for the base metal and deposition (256 and 362.5 respectively), the mismatch ratio is calculated to be 1.31 (overmatched). Higher hardness is positively correlated to higher yield strengths, with both properties having been shown to follow a Hall-Petch relationship with respect to grain size [13–15]. The relationship between hardness ( $H$ ) and yield strength ( $\sigma_y$ ) has been shown to approximately follow,

$$\sigma_y = \frac{H}{3} (B)^{m-2} \quad (4)$$

where  $B$  is an experimentally determined constant based on the strain at the 0.2% offset yield point and  $m$  is the Meyer's hardness coefficient [16]. Good accuracy has been demonstrated in literature between hardness mismatch ratios and strength mismatch ratios for overmatched and matched systems [17], suggesting that the use of microhardness to determine the extent of mismatch is typically acceptable.

Although hardness measurements indicate that the ESD Inconel 718 is overmatched, the use of medium ESD process parameters produce a repaired specimen with a lower yield strength than the base metal specimen. This is contrary to what is expected based on Equation 4, although similar results have been reported in literature for Inconel 718 laser welded joints with a hardness mismatch of 1.30 and a reduction in yield strength of 4% [18]. This disconnect between the expected and experimental result can be attributed to yield strength anisotropy. Materials tested perpendicular to the build-up direction – as in ESD repaired cavities – are shown to exhibit lower yield strengths based on literature results of selective laser melted or electron beam melted materials with textured columnar grains [19,20]. In several literature studies, hardness measurements show no or minimal anisotropy (5%) – as was found for medium energy ESD repaired cavities (4.2%) – while yield strength anisotropy is significant (35%) [21,22]. This suggests that the use of microhardness to determine strength mismatch ratios or tensile properties may not be applicable in directionally solidified materials with highly textured grains, a conclusion that has previously been explicitly reported for additive manufactured materials [22]. Based on the elongated grain structures, directional solidification conditions in ESD, and inconsistency between the hardness mismatch ratio and yield strength presented in this work, yield strength anisotropy likely extends to ESD materials as well.

Cracks initiating in the weld metal, in this case likely due to the presence of brittle secondary phases [23], tend to propagate in the direction of greatest plastic strain concentration [24]. The highest plastic strain concentration – as measured by grain elongation and hardness changes during tensile testing (Figure 5 and 6) – is located in the base metal on the plane through the center of the repaired cavity, where the specimen's cross-sectional area is the smallest. This can be seen in Figure 7b, where the bottom of the specimen exhibits necking as a result of plastic deformation. As was confirmed by the calculation of an adjusted ultimate strength in Table 4, the pre-failure crack within the deposition does not propagate into or otherwise affect the base metal substrate of repaired specimens. Work published in literature attributes this result to a greater fracture toughness in the lower strength material [24].

#### 4.2. Effect of Microstructure on Crack Propagation and Fracture Toughness

When fracture of the deposited material occurs, propagation of the crack is redirected by splat boundaries. A cross-sectional image of the fracture surface (Figure 8) shows the step-like facets caused by two primary directions of crack propagation.

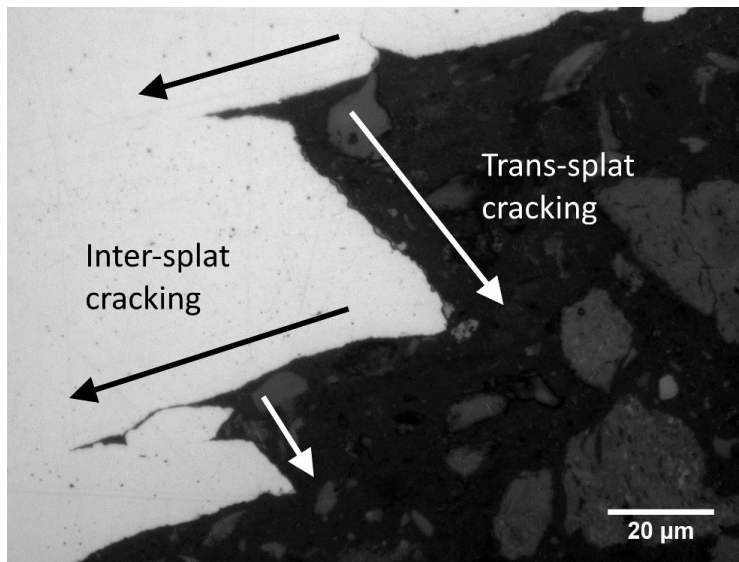


**Figure 8.** Cross sectional OM image of fracture surface showing inter-splat and trans-splat cracking

Previously, Figure 5b displayed the fracture surface of the deposited material with the formation of step-like facets. Several secondary cracks can be seen along the splat boundaries on the step facets, visible in Figure 5b and more clearly seen in Figure 8 along the inter-splat cracking direction. The presence of step facets and secondary cracks suggest that crack propagation occurring along a splat boundary (inter-splat) is met with varying resistance (fracture toughness), occasionally encouraging crack propagation through the splat (trans-splat). This mixed cracking mechanism results in step facet formation similar to previously reported metals with lamellar structures [25]. Evidence of secondary inter-splat cracking is only found branching from the fracture surface as seen in Figure 8, with the rest of the deposition free from these cracks.

The occurrence of crack propagation at two primary angles to the applied tensile stress, corresponding with cracking in the inter-splat direction and in the trans-splat direction, suggest differences in the fracture toughness between the interfaces and splats of ESD materials. The relative resistance to crack propagation can be determined by considering the relative energy dissipated during fracture for each crack propagation angle. Considering that both trans-splat and inter-splat cracks propagate at angles other than 90° from the applied stress, mixed mode effects must be considered. The applied stress ( $\sigma_0$ ) can be broken down into Mode I ( $\sigma_I$ ) and Mode II ( $\sigma_{II}$ ) components, as shown in Figure 9 and by Equations 5 and 6. Mode I corresponds to stress acting perpendicular to the crack face, while Mode II refers to an in-plane shear perpendicular to Mode I in the direction of crack propagation.

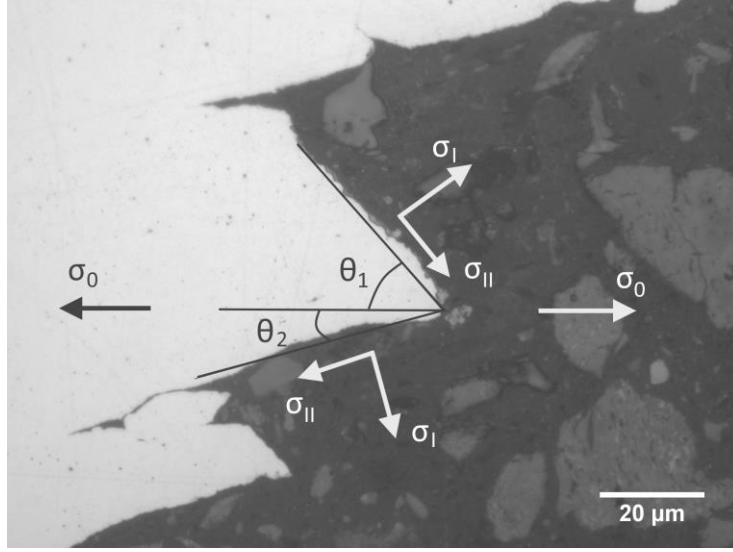


**Figure 9.** Examples of  $\sigma_I$ ,  $\sigma_{II}$ , and  $\theta$  for trans-splat ( $\theta_1$ ) and inter-splat ( $\theta_2$ ) cracks

$$\sigma_I = \sigma_0 \sin^2(\theta) \quad (5)$$

$$\sigma_{II} = \sigma_0 \sin(\theta)\cos(\theta) \quad (6)$$

Stress intensity factors (SIF) are used to describe the stress state at the crack tip caused by the Mode I and Mode II stresses. When the stress intensity factor at the tip of a crack reaches a critical value, fracture occurs as the crack propagates through the material. The stress intensity factor caused by Mode I loading ( $K_I$ ) and Mode II loading ( $K_{II}$ ) can be determined from the individual Mode I and Mode II stress components as shown in Equations 7 and 8,

$$K_I = f \sigma_I \sqrt{\pi a} \quad (7)$$

$$K_{II} = f \sigma_{II} \sqrt{\pi a} \quad (8)$$

where  $a$  is the crack length for an edge crack and  $f$  is a geometry dependent factor equal in this case to 1.122 [26]. Stress intensity factors can be used to determine the energy release rate ( $G$ ), with the critical value of  $G$  required for crack propagation known as the fracture toughness [27]. In order for a crack to propagate through a material, energy release must equal or exceed that required to form new surfaces at the tip of the crack. Therefore, the higher the energy release rate required for crack propagation, the higher the fracture toughness of the material. Equation 9 relates the energy release rate to the Mode I and Mode II stress intensity factors,

$$G = \frac{1 - \nu^2}{E} [K_I^2 + K_{II}^2] \quad (9)$$

where  $\nu$  is Poisson's ratio and  $E$  is Young's Modulus. The model presented here is based on linear elastic theory, which assumes the material is linear elastic and isotropic in the direction of crack propagation. Much work has been done to understand crack kinking away from interfaces and crack deflection at interfaces [28]. In either case, the relative value of the energy release rates for a crack propagating through a splat ( $G_{splat}$ ) or along an interface ( $G_{int}$ ) can be used to assess which of the two scenarios is most likely. The ratio is as defined in Equation 10 for an interface within a homogeneous material (the same Young's modulus and Poisson's ratio on either side of the interface).

$$\frac{G_{int}}{G_{splat}} = \frac{K_{I int}^2 + K_{II int}^2}{K_{I splat}^2 + K_{II splat}^2} \quad (10)$$

Calculations of the energy release rate ( $G$ ) at various angles is performed using Equation 10 and the result is shown in Figure 10. As expected, energy release rate increases for higher propagation angles with primary Mode I loading, and decreases at lower angles where Mode II loading has a higher influence. A comparison of energy release rates between the two angles of propagation in ESD Inconel 718 (average of 45° for trans-splat and 23° for inter-splat) show a 0.291  $G_{int}/G_{bulk}$  ratio. This suggests that splat boundaries of ESD Inconel 718 have a critical energy release rate (fracture toughness) approximately 30% that of the splat material inside the boundaries.

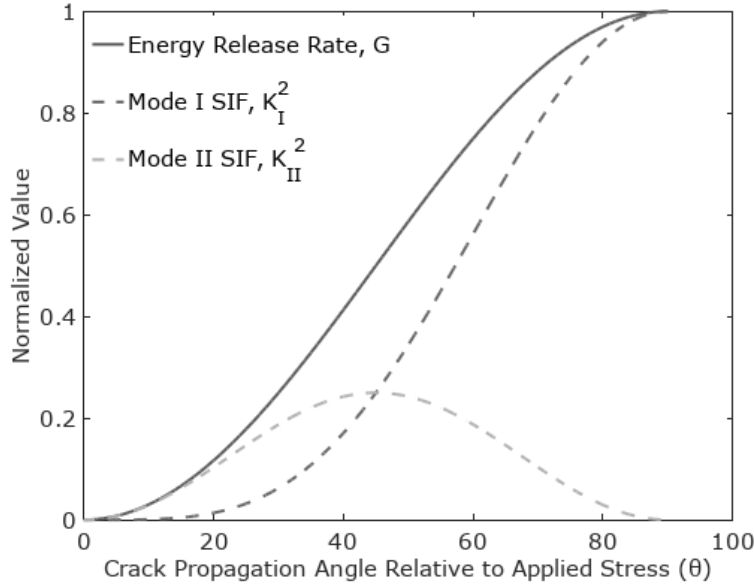


**Figure 10.** Energy release rate dependence on crack propagation angle and contributing stress intensity factors

In the case that a crack is propagating towards an interface, the inequality in Equation 11 must hold for the crack to deflect along the interface. An interface fracture toughness less than 0.291 times the fracture toughness of the bulk material will cause deflection. However, an interface fracture toughness greater than 0.291 times the splat fracture toughness will result in penetration across the interface. This inequality can also be used to describe the reverse scenario, in which a crack propagating along an interface may kink into the splat. The inequality in Equation 11 would hold for a crack that continues to propagate along the interface, whereas the reverse inequality describes the situation in which a crack propagating along an interface kinks into the splat material.

$$G_{int} < 0.291G_{splat} \quad (11)$$

#### 4.3. Effect of Microstructure on Tensile Properties

Several microstructure features associated with ESD can be used to explain the performance of repaired cavities under tensile stress. Low energy ESD parameters result in more splat boundaries, which were found to be more readily revealed during etching than grain boundaries (1.5 minutes vs. 2.5 minutes of etching required, respectively). More reactive boundary atoms are dissolved by etchants at a faster rate than those within the boundaries, with the etching rate affected by concentration of dislocation induced lattice distortions or impurity atoms [29,30]. Increasing the number of boundaries acting as obstacles to dislocation movement is known to have a positive effect on yield strength [29], which suggests that an increase in the number of splats and splat boundaries contribute to the observed increase in yield strength for low energy ESD repaired specimens. Literature studies have also demonstrated improved mechanical performance as a result of finer subgrain size [31], which is shown in Figure 3

to depend on splat thickness. This is also expected to contribute to the increase in yield strength for low energy ESD repairs.

Although defects at boundaries have the positive effect of improving the yield strength of repaired specimens, they also reduce dislocation mobility and increase localized stresses. These localized stresses have been shown to facilitate crack propagation along boundaries [32]. The dislocation density at the boundary is expected to vary, depending on the grain misorientation between splats. As was shown previously in Figure 2c, some grains extend across splat boundaries, suggesting a lower dislocation density at these locations. This reduction in defects is expected to increase the fracture toughness and induce a change in crack propagation from the inter-splat direction to the trans-splat direction.

In addition to variations in fracture toughness along splat boundaries, the material within a splat is also expected to vary in its fracture toughness. Thicker deposition splats result in coarser grain structures and increased segregation of an interconnected Laves phase, similar to higher energy input in other solidification processes [33]. Interdendritic regions with Laves phase precipitation are expected to be detrimental to the ultimate strength and fracture toughness of the ESD Inconel 718, however are not expected to detrimentally affect the yield strength in the as-deposited condition. Literature has shown the quantity of Laves phase in pre-precipitation hardened Inconel 718 to have no effect on the room temperature yield strength while negatively impacting the ultimate strength and ductility [34]. Laves phases are reported to have lower fracture toughness than the surrounding matrix, while preventing the formation of strengthening  $\gamma''$  phases during precipitation hardening by removal of alloying elements from the nickel matrix [33–35]. Therefore, the thickness of a deposited splat is indirectly expected to vary the trans-splat fracture toughness and mechanical properties such as ultimate strength and ductility.

Variations in fracture toughness and mechanical properties at splat boundaries (attributed to dislocation density) and in the splat (attributed to subgrain microstructure size and Laves phase formation), are expected to account for the mixed inter-splat and trans-splat crack propagation mechanism. A trade-off exists as a result of the unique splat microstructure of ESD materials. An increase in the number of splat boundaries and higher microhardness from smaller subgrain sizes in thinner splats is identified as the reason for the yield strength increase in lower energy ESD repaired cavities, a beneficial property for repair applications due to the tendency to operate within the elastic region of a material. However, splat boundaries exhibit a fracture toughness of approximately 30% of the material within the splat bulk. This microstructure influenced crack propagation pathway, along with the presence of a brittle Laves phase, is expected to contribute to earlier fracture when compared to an Inconel 718 material of equivalent hardness with no splat interfaces or laves phases. Lower energy ESD can be expected to have more splat boundaries – making inter-splat fracture more likely – while also increasing the fracture toughness of trans-splat cracking due to less Laves phase formation. This trade-off likely explains the lack of statistically significant difference in ultimate strength ( $p=0.805$ ) between the low energy and medium energy ESD process parameters used to repair specimen cavities.

## Conclusions

Mechanical properties of repaired Inconel 718 specimens were found to be dependent on microstructure, which is a result of the ESD process parameters used. The effect of ESD microstructure on yield strength and fracture toughness can be summarized as follows:

1. ESD splat boundaries and subgrain microstructure size are correlated to yield strength recovery. Cavities repaired with low energy ESD parameters are known to result in thinner splats, leading to an increased number of splat boundaries and finer subgrain microstructures. The splat boundaries are expected to act as barriers to dislocation movement which – in combination with the higher strength of finer subgrains – contributes to the observed increase in yield strength.
2. ESD splat boundaries have lower fracture toughness than material within the splat. Crack propagation angles obtained from fractured surfaces indicate that the fracture toughness of splat boundaries is approximately 30% that of the splat material. High dislocation densities and high localized stresses at splat boundaries are expected to contribute to the lower fracture toughness.
3. The observed combination of trans-splat and inter-splat cracking directions, in which cracks propagate through splats and along splat boundaries, suggest that fracture toughness is not constant along boundaries or in the

splats. The variation in fracture toughness along splat boundaries is attributed to grains which traverse splat boundaries and decrease dislocation density, while the variation in fracture toughness within the splat is attributed to differences in laves phase formation during the ESD process.

## Acknowledgements

This work was performed with funding support from the Natural Sciences and Engineering Research Council of Canada (NSERC) and Huys Industries, in collaboration with the Centre for Advanced Materials Joining and the Multi-Scale Additive Manufacturing Lab at the University of Waterloo.

## References

- [1] P. Leo, G. Renna, G. Casalino, Study of the direct metal deposition of AA2024 by electrospark for coating and reparation scopes, *Appl. Sci.* 7 (2017). doi:10.3390/app7090945.
- [2] C.J. Chen, M.C. Wang, D.S. Wang, H.S. Liang, P. Feng, Characterisations of electrospark deposition Stellite 6 alloy coating on 316L sealed valve used in nuclear power plant, *Mater. Sci. Technol.* 26 (2010) 276–280. doi:10.1179/174328409X430447.
- [3] B.D. Sartwell, K.O. Legg, N. Price, D. Aylor, V. Champagne, M. Pepi, T. Pollard, Electrospark Deposition for Depot- and Field-Level Component Repair and Replacement of Hard Chromium Plating, *Environ. Secur. Technol. Certif. Progr.* (2006) 299. <http://www.dtic.mil/docs/citations/ADA603502>.
- [4] A. Carofalo, V. Dattoma, R. Nobile, F.W. Panella, G. Alfeo, A. Scialpi, G.P. Zanon, Mechanical Characterization of a Nickel-based Superalloy Repaired using MicroPlasma and ESD Technology, *Procedia Eng.* 109 (2015) 312–319. doi:10.1016/j.proeng.2015.06.238.
- [5] J. Filliben, A. Heckert, NIST Dataplot, (2016). <https://www.itl.nist.gov/div898/software/dataplot/refman2/auxillar/hedgeg.htm>.
- [6] G.M. Sullivan, R. Feinn, Using Effect Size—or Why the P Value Is Not Enough, *J. Grad. Med. Educ.* 4 (2012) 279–282. doi:10.4300/JGME-D-12-00156.1.
- [7] J.A. Durlak, How to Select, Calculate, and Interpret Effect Sizes, *J. Pediatr. Psychol.* 34 (2009) 917–928. doi:10.1093/jpepsy/jsp004.
- [8] M. Fakoori Hasanabadi, F. Malek Ghaini, M. Ebrahimnia, H.R. Shahverdi, Production of amorphous and nanocrystalline iron based coatings by electro-spark deposition process, *Surf. Coat. Technol.* 270 (2015) 95–101. doi:10.1016/j.surfcoat.2015.03.016.
- [9] K.R. Vishwakarma, O.A. Ojo, N.L. Richards, Nano-size solidification microconstituents in electro-spark deposited Ni-base superalloy, *Philos. Mag. Lett.* 95 (2015) 30–36. doi:10.1080/09500839.2014.995740.
- [10] P. Guo, X. Lin, J. Li, Y. Zhang, M. Song, W. Huang, Electrochemical behavior of Inconel 718 fabricated by laser solid forming on different sections, *Corros. Sci.* (2017) 0–1. doi:10.1016/j.corsci.2017.12.021.
- [11] S.H. Baghjari, F. Malek Ghaini, H.R. Shahverdi, C. Mapelli, S. Barella, D. Ripamonti, Laser welding of niobium to 410 steel with a nickel interlayer produced by electro spark deposition, *Mater. Des.* 107 (2016) 108–116. doi:10.1016/j.matdes.2016.06.022.
- [12] R.K. GUPTA, C. Mathew, P. Ramkumar, Strain Hardening in Aerospace Alloys, *Front. Aerosp. Eng.* 4 (2015) 1–13. doi:10.12783/fae.2015.0401.01.
- [13] T. Hanamura, H. Qiu, *Analysis of Fracture Toughness Mechanism in Ultra-fine-grained Steels*, Springer Japan, Tokyo, 2014. doi:10.1007/978-4-431-54499-9.
- [14] E.O. Hall, The Deformation and Ageing of Mild Steel: III Discussion of Results, *Proc. Phys. Soc. London Sect. B.* 64 (1951) 747–753. doi:10.1088/0370-1301/64/9/303.

- [15] N.J. Petch, The cleavage strength of polycrystals, *J. Iron Steel Inst.* 174 (1953) 25–28.
- [16] J.R. Cahoon, W.H. Broughton, A.R. Kutzak, The determination of yield strength from hardness measurements, *Metall. Trans.* 2 (1971) 1979–1983. doi:<https://doi.org/10.1007/BF02913433>.
- [17] Y. Chiba, K. Murayama, S. Satoh, K. Miyashiro, M. Ohata, F. Minami, Strength-mismatch effect on steel weld HAZ-toughness in CTOD and Charpy tests, *Weld. World.* 54 (2010) 147–153. doi:[10.1007/BF03263500](https://doi.org/10.1007/BF03263500).
- [18] X. Cao, B. Rivaux, M. Jahazi, J. Cuddy, A. Birur, Effect of pre- and post-weld heat treatment on metallurgical and tensile properties of Inconel 718 alloy butt joints welded using 4 kW Nd:YAG laser, *J. Mater. Sci.* 44 (2009) 4557–4571. doi:[10.1007/s10853-009-3691-5](https://doi.org/10.1007/s10853-009-3691-5).
- [19] L. Thijs, M.L. Montero Sistiaga, R. Wauthle, Q. Xie, J.P. Kruth, J. Van Humbeeck, Strong morphological and crystallographic texture and resulting yield strength anisotropy in selective laser melted tantalum, *Acta Mater.* 61 (2013) 4657–4668. doi:[10.1016/j.actamat.2013.04.036](https://doi.org/10.1016/j.actamat.2013.04.036).
- [20] C. Körner, H. Helmer, A. Bauereiß, R.F. Singer, Tailoring the grain structure of IN718 during selective electron beam melting, *MATEC Web Conf.* 14 (2014) 8001. doi:[10.1051/mateconf/20141408001](https://doi.org/10.1051/mateconf/20141408001).
- [21] A.A. Deev, P.A. Kuznetsov, S.N. Petrov, Anisotropy of Mechanical Properties and its Correlation with the Structure of the Stainless Steel 316L Produced by the SLM Method, *Phys. Procedia.* 83 (2016) 789–796. doi:[10.1016/j.phpro.2016.08.081](https://doi.org/10.1016/j.phpro.2016.08.081).
- [22] L. Hitzler, J. Hirsch, B. Heine, M. Merkel, W. Hall, A. Öchsner, On the anisotropic mechanical properties of selective laser-melted stainless steel, *Materials (Basel).* 10 (2017). doi:[10.3390/ma10101136](https://doi.org/10.3390/ma10101136).
- [23] R. Cortés, E.R. Barragán, V.H. López, R.R. Ambriz, D. Jaramillo, Mechanical properties of Inconel 718 welds performed by gas tungsten arc welding, *Int. J. Adv. Manuf. Technol.* (2017). doi:[10.1007/s00170-017-1128-x](https://doi.org/10.1007/s00170-017-1128-x).
- [24] H. Peter, U. Zerbst, Recent Trends in Fracture and Damage Mechanics, in: *Recent Trends Fract. Damage Mech.*, 2016: pp. 61–86. doi:[10.1007/978-3-319-21467-2](https://doi.org/10.1007/978-3-319-21467-2).
- [25] J. Yang, H. Li, D. Hu, M. Dixon, Microstructural characterisation of fatigue crack growth fracture surfaces of lamellar Ti45Al2Mn2Nb1B, *Intermetallics.* 45 (2014) 89–95. doi:[10.1016/j.intermet.2013.10.011](https://doi.org/10.1016/j.intermet.2013.10.011).
- [26] H. Tada, P. Paris, G. Irwin, Stress Analysis Results for Common Test Specimen Configurations, in: *Stress Anal. Cracks Handbook*, Third Ed., ASME, Three Park Avenue New York, NY 10016-5990, NY 10016-5990, 2017: pp. 39–80. doi:[10.1115/1.801535.ch2](https://doi.org/10.1115/1.801535.ch2).
- [27] J.W. Hutchinson, STRESSES AND FAILURE MODES IN THIN FILMS AND MULTILAYERS, Notes a Dcamm Course. Tech. Univ. Denmark. (1996) 45.
- [28] H. Ming-Yuan, J.W. Hutchinson, Crack deflection at an interface between dissimilar elastic materials, *Int. J. Solids Struct.* 25 (1989) 1053–1067. doi:[10.1016/0020-7683\(89\)90021-8](https://doi.org/10.1016/0020-7683(89)90021-8).
- [29] W. Callister, D. Rethwisch, *Materials science and engineering: an introduction*, 2007. doi:[10.1016/0025-5416\(87\)90343-0](https://doi.org/10.1016/0025-5416(87)90343-0).
- [30] D. Hull, D.J. Bacon, *Introduction to Dislocations*, Fifth, Elsevier, Oxford, 2011. doi:[10.1016/C2009-0-64358-0](https://doi.org/10.1016/C2009-0-64358-0).
- [31] Y. Ruan, A. Mohajerani, M. Dao, Microstructural and Mechanical-Property Manipulation through Rapid Dendrite Growth and Undercooling in an Fe-based Multinary Alloy, *Sci. Rep.* 6 (2016) 1–11. doi:[10.1038/srep31684](https://doi.org/10.1038/srep31684).
- [32] R.A. Mirshams, C.H. Xiao, S.H. Whang, W.M. Yin, R-Curve characterization of the fracture toughness of

nanocrystalline nickel thin sheets, *Mater. Sci. Eng. A.* 315 (2001) 21–27. doi:10.1016/S0921-5093(01)01213-8.

- [33] M. Ma, Z. Wang, X. Zeng, Effect of energy input on microstructural evolution of direct laser fabricated IN718 alloy, *Mater. Charact.* 106 (2015) 420–427. doi:10.1016/j.matchar.2015.06.027.
- [34] J.J. Schirra, R.H. Caless, R.W. Hatala, The Effect of Laves Phase on the Mechanical Properties of Wrought and Cast + HIP Inconel 718, in: *Superalloys 718, 625 Var. Deriv.*, TMS, 1991: pp. 375–388. doi:10.7449/1991/Superalloys\_1991\_375\_388.
- [35] E.L. Stevens, J. Toman, A.C. To, M. Chmielus, Variation of hardness, microstructure, and Laves phase distribution in direct laser deposited alloy 718 cuboids, *Mater. Des.* 119 (2017) 188–198. doi:10.1016/j.matdes.2017.01.031.